Reaction Chemistry & Engineering

ROYAL SOCIETY OF CHEMISTRY

PAPER

Published on 28 July 2026

Cite this: DOI: 10.1039/d6re00101g

A unified kinetic model with pressure-dependent unimolecular falloff for COS thermal pyrolysis

Klaus Jacobs, [a] Soroush Zareghorbaei, [a] Jeroen Lauwaert [b] and Joris W. Thybaut *[a]

Carbonyl sulfide (COS) is an environmentally relevant sulfur pollutant and a potential precursor for carbon monoxide and elemental sulfur production *via* high-temperature processes. Reliable kinetic models are therefore needed for reactor design and process analysis, yet available descriptions remain fragmented across limited concentration ranges and inconsistent mechanistic assumptions. In this work, a compact reactor-scale kinetic model for COS thermal pyrolysis was developed and evaluated over a temperature range of 750–1255 °C and inlet COS mole fractions from 0.156 to 100%. The model reconciles four independent literature datasets within a reaction network including pressure-dependent unimolecular decomposition, reversible bimolecular COS decomposition, and sulfur-mediated interconversion steps. The unimolecular pathway was described using a QRRK-based falloff expression obtained independently from direct rate-coefficient data, while the forward and reverse bimolecular parameters were estimated simultaneously from the complete COS conversion dataset. The final model reproduced the combined dataset with strong statistical performance, giving R^2 = 97.5%. Pathway analysis showed that COS conversion is governed mainly by bimolecular COS consumption at lower temperatures and higher COS availability, whereas unimolecular decomposition becomes increasingly competitive at higher temperatures and as COS is depleted. Reverse COS formation becomes important primarily under concentrated-feed conditions, while sulfur interconversion indirectly influences conversion by controlling the S/S_2 pool. Monte Carlo propagation of fitted-parameter uncertainty indicated that the final predictions are statistically stable within the investigated operating window. The resulting model provides a compact and physically interpretable kinetic description suitable for reactor-scale simulations, while highlighting the need for future experiments with improved sulfur-species and product characterization.

Received 26th March 2026,
Accepted 27th July 2026

DOI: 10.1039/d6re00101g

rsc.li/reaction-engineering

1. Introduction

In the chemical and petrochemical industries, sulfur recovery is commonly carried out through the Claus process, in which hydrogen sulfide (H_2S), originating from sour natural gas and refinery gas streams, is converted into elemental sulfur.[1] Under the high-temperature conditions of these processes, carbonyl sulfide (COS) can be formed through side reactions involving COx and sulfur-containing species.[2] Because COS is more difficult to remove than H_2S, its presence complicates downstream sulfur management. Although catalytic hydrolysis can convert COS into CO_2 and H_2S, this route is subject to both kinetic and thermodynamic limitations, which may result in incomplete COS removal and residual sulfur-containing emissions.[3,4] As a result, COS is traditionally regarded as an undesirable intermediate in industrial sulfur treatment. In the e-CODUCT process concept,[5] however, COS is not treated solely as a byproduct but as a desired intermediate in a sulfur valorization pathway. In this concept, CO_2 and H_2S are first converted into COS (and water),[6] which is subsequently thermally decomposed into carbon monoxide (CO) and elemental sulfur (S_x). This reaction route is attractive because it proceeds in the absence of oxygen and yields products with direct industrial value, while potentially avoiding some of the limitations associated with conventional hydrolysis-based removal routes. The successful development of such a process, however, requires a reliable kinetic description of COS pyrolysis over a broad range of temperatures, pressures, and feed compositions. Although numerous works have investigated COS decomposition under different thermal conditions,[7–12] the reported kinetics remain fragmented, reflecting differences in reactor configuration, operating regime, and mechanistic interpretation. This

[a] *Laboratory for Chemical Technology (LCT), Ghent University, Technologiepark 125, 9052 Ghent, Belgium. E-mail: Joris.Thybaut@UGent.be*
[b] *Industrial Catalysis and Adsorption Technology (INCAT), Ghent University, Valentin Vaerwyckweg 1, 9000 Ghent, Belgium*

motivates the development of a more consistent kinetic framework for COS thermal decomposition.

To enable accurate kinetic modeling of COS pyrolysis, it is essential to account for the full range of plausible gas-phase reaction pathways that may occur when COS is thermally processed in the absence of oxygen. These include not only unimolecular decomposition, but also bimolecular reactions, sulfur abstraction steps, and sulfur recombination mechanisms, all of which have been observed or proposed under varying experimental conditions. Depending on the feed composition, COS pyrolysis may occur from pure COS feeds to diluted gas mixtures, as often encountered in industrial settings where COS is present as a trace byproduct in high-temperature gas streams. A robust reaction network must therefore represent the various pathways that possibly dominate across this range of operating conditions. Based on experimental evidence and kinetic investigations available in the literature,[2,7,9–17] a literature-based set of candidate reactions was assembled for COS pyrolysis. These candidate pathways are summarized in Table 1 and serve as the starting point for identifying the dominant reactions that can be meaningfully evaluated from the available COS conversion data.

Although COS decomposition has been investigated in several experimental studies, the available kinetic descriptions remain fragmented. Early shock-tube investigations treated COS decomposition mainly as a pressure-dependent unimolecular gas-phase process represented as reaction 1 in Table 1, in which collisional activation by a third body controls the apparent rate under low-pressure conditions.[7–9] Hay and Belford[8] represented this behavior using a Kassel-type expression derived from (Rice–Ramsperger–Kassel) RRK concepts, whereas Schecker and Wagner[7] and Woiki and Roth[9] reported low-pressure Arrhenius-type parameterizations for the apparent unimolecular rate coefficient. More recently, Panda *et al.*[17] reported pressure-dependent rate coefficients for OCS decomposition in different bath gases and described the falloff behavior using a classical RRK formulation. These studies establish the importance of pressure dependence for unimolecular COS decomposition, but they mainly describe conditions where this pathway dominates and do not by themselves provide a unified reactor-scale kinetic model across the lower-temperature and broader feed-composition range relevant to COS pyrolysis applications.

Flow-reactor investigations indicate that unimolecular decomposition alone is insufficient under several practically relevant conditions. Karan *et al.*[10] investigated COS decomposition at lower temperatures and near-atmospheric pressure and observed that COS conversion increased with inlet COS concentration, which is inconsistent with a purely unimolecular first-order description at fixed temperature, pressure, and residence time. This behavior motivated the inclusion of concentration-dependent bimolecular COS consumption pathways (reaction 2, forward). Karan *et al.*[11] also investigated the reverse formation of COS from CO and sulfur (reaction 2, reverse), showing that reversible COS formation can become relevant under product-rich or concentrated-feed conditions. Additional sulfur-mediated pathways, including sulfur abstraction from COS (reaction 3) and sulfur recombination/dissociation reactions (reaction 4), have also been proposed or parameterized in the literature.[12,16,18,19] Other minor reactions leading to CO_2,

Table 1 Reported reaction steps involved in COS decomposition

#	Reaction	Rate expression	Pre-exponential factor	m	n	Ea/E_0 (kJ mol^{-1})	Ref.
1	COS + M → CO + S + M	$r_1 = k_1 C_{COS} C_M$	1.11×10^5 (m^3 mol^{-1} s^{-1} K$^{-0.5}$)	0.5	1.87	299[b]	8
			1×10^9 (m^3 mol^{-1} s^{-1})	0	0	255	7
			2.9×10^8 (m^3 mol^{-1} s^{-1})	0	0	266	9
			3×10^8 (m^3 mol^{-1} s^{-1})	0	0	245	16
		$r_1 = k_1 C_{COS}{}^a$	4.99×10^{11} (s^{-1})	0	0	283[b]	17
2	COS + COS ⇌ 2CO + S_2	$r_{2f} = k_{2f} C_{COS}{}^2$	4.39×10^9 (m^3 mol^{-1} s^{-1})	0	0	197	10
			1×10^7 (m^3 mol^{-1} s^{-1})	0	0	180	8
		$r_{2f} = k_{2f} C_{COS}{}^{1.5} C_M{}^{0.5}$	2.22×10^7 (m^3 mol^{-1} s^{-1})	0	0	170	10
		$r_{2r} = k_{2r} C_{COS} C_{S_2}$	318 (m^3 mol^{-1} s^{-1})	0	0	56	11
3	COS + S → CO + S_2	$r_3 = k_3 C_{COS} C_S$	2.35×10^6 (m^3 mol^{-1} s^{-1})	0	0	28.3	12
			2.2×10^6 (m^3 mol^{-1} s^{-1})	0	0	34.8	16
			430 (m^3 mol^{-1} s^{-1} K$^{-3.68}$)	3.68	0	4.4	16
4	S_2 + M ⇌ 2S + M	$r_{4f} = k_{4f} C_{S_2} C_M$	3×10^9 (m^3 mol^{-1} s^{-1})	0	0	425	18, 19
		$r_{4r} = k_{4r} C_S{}^2$	5.5×10^4 (m^3 mol^{-1} s^{-1})	0	0	3.45	19
5	COS + COS ⇌ 2CO + 2S	—	—	—	—	—	8
6	COS + COS → 2S + CO_2 + C	—	—	—	—	—	15
7	COS + COS ⇌ CO_2 + CS_2	—	—	—	—	—	13, 15, 20, 21
8	COS + S_2 → CO + S_3	—	—	—	—	—	10
9	COS + S → CS + SO	—	—	—	—	167–217	8

Reaction rate coefficient is calculated based on this general formula $k = AT^m \left(\frac{Ec}{RT}\right)^n e^{\left(-\frac{Ec}{RT}\right)}$. [a] unimolecular rate constant calculated using classical RRK expression. [b] Correspond to E_0, an effective critical/threshold energy used in RRK/Kassel-type falloff formulations, rather than to an apparent Arrhenius activation energy Ea.

CS_2, or higher sulfur species have been reported or discussed, especially outside the main temperature and composition range considered here.[8,13,15,20,21] Together, these studies show that COS pyrolysis cannot be represented by a single universal rate expression across all regimes.

A practical kinetic model for reactor simulations should therefore combine two features that are currently not available in a simultaneous manner. First, the unimolecular decomposition step should retain explicit pressure dependence, because the apparent rate coefficient changes with bath-gas concentration and approaches different limiting behavior in the low- and high-pressure regimes.[22–25] Second, the model should include the COS-concentration-dependent pathways needed to reproduce flow-reactor conversion data, where longer residence times and higher COS concentrations can increase the contribution of bimolecular and sulfur-mediated chemistry.[26,27] A full *ab initio* RRKM/master-equation treatment of all relevant reactions would provide a more detailed elementary description, but for COS this would require reliable potential-energy surfaces, transition states, collisional energy-transfer parameters, and, for the low-energy CO + S(^{3}P) channel, non-adiabatic information involving singlet–triplet coupling. Such a treatment is beyond the scope of the present reactor-oriented model.

The objective of this work is to develop a unified, pressure-dependent kinetic model for COS thermal pyrolysis that reconciles the dominant trends reported across independent literature datasets. The unimolecular decomposition step is described using a quantum RRK formulation, fitted independently to pressure-dependent direct-rate data from Hay and Belford,[8] Schecker and Wagner,[7] and Panda *et al.*[17] The optimized, pressure-dependent $k_1(T,[M])$ expression is then kept fixed in the reactor-model regression, while the remaining identifiable parameters associated with bimolecular COS consumption and reverse COS formation are estimated from published COS conversion data. In this way, the pressure dependence of the unimolecular decomposition step is regressed by independent direct-rate measurements, whereas the reactor data are used to identify the additional pathways required to reproduce conversion over the experimentally investigated range.

The resulting model is validated against four literature datasets spanning 750–1255 °C, 100–140 kPa, COS feed mole fractions from 0.156 to 100%, and residence times from 0.5 to 48 s.[2,10,14,16] The analysis clarifies the conditions under which unimolecular decomposition, bimolecular COS consumption, sulfur-mediated chemistry, and reverse COS formation contribute to the observed conversion. The model is therefore not intended as a complete elementary RRKM/master-equation mechanism, but as a comprehensive and mechanistically guided kinetic framework for the dominant experimentally resolvable gas-phase pathways. By providing a compact pressure-dependent description suitable for reactor-scale simulations, this work aims to enable the modelling of industrially relevant reactors in which COS decomposition is significant, including high-temperature sulfur-containing gas streams and emerging COS-based sulfur-valorization processes.

2. Methods

2.1. Selection of steady-flow reactor datasets for conversion modelling

For the kinetic model development, four literature reported experimental datasets were selected based on their level of detail and consistency, rendering them the most reliable sources available for this purpose.[2,10,14,16] A key selection criterion was the reactor type employed: all investigations used isothermal reactors under the specified operating conditions. Among these, only Faraji *et al.*[14] employed a packed-bed configuration with inert materials, while the others used empty tubular reactors. The use of tubular reactors was considered essential because they provide a more controlled environment for steady-state reaction kinetics, particularly over extended residence times. In contrast to shock-tube reactors, where reactions occur under highly transient, high-temperature, and short-duration conditions, tubular reactors allow for better-defined temperature profiles and more accurate measurements of conversion over time.

In addition to tubular reactors, one dataset based on a jet-stirred reactor (JSR) was also included,[16] which operates under ideal continuous stirred tank reactor (CSTR) conditions. The inclusion of this CSTR-type data is justified by its ability to provide complementary kinetic information under well-mixed, isothermal conditions, particularly at low reactant feed composition (0.156%). These conditions reduce temperature and concentration gradients, enhancing the reliability of intrinsic kinetic measurements.

The extracted dataset comprises 60 experiments conducted across a wide range of temperatures (750–1255 °C), pressures (100–140 kPa), COS feed mole fractions (0.00156 to 1.0), and residence times (0.5 to 48 s). Fig. 1. provides an overview of the selected experiments by plotting COS conversion as a function of inlet COS mole fraction on a logarithmic scale. Marker shape identifies the literature source, while color denotes temperature in the left panel and ln(residence time/s) in the right panel. The detailed input used for every experimental data point can be found in SI.

2.2. Selection of relevant reactions and identifiable kinetic parameters

To construct a kinetic model that remains chemically meaningful and statistically identifiable, the reaction network was selected from the literature-reported pathways summarized in Table 1. The selection was based on three criteria: chemical plausibility under the investigated

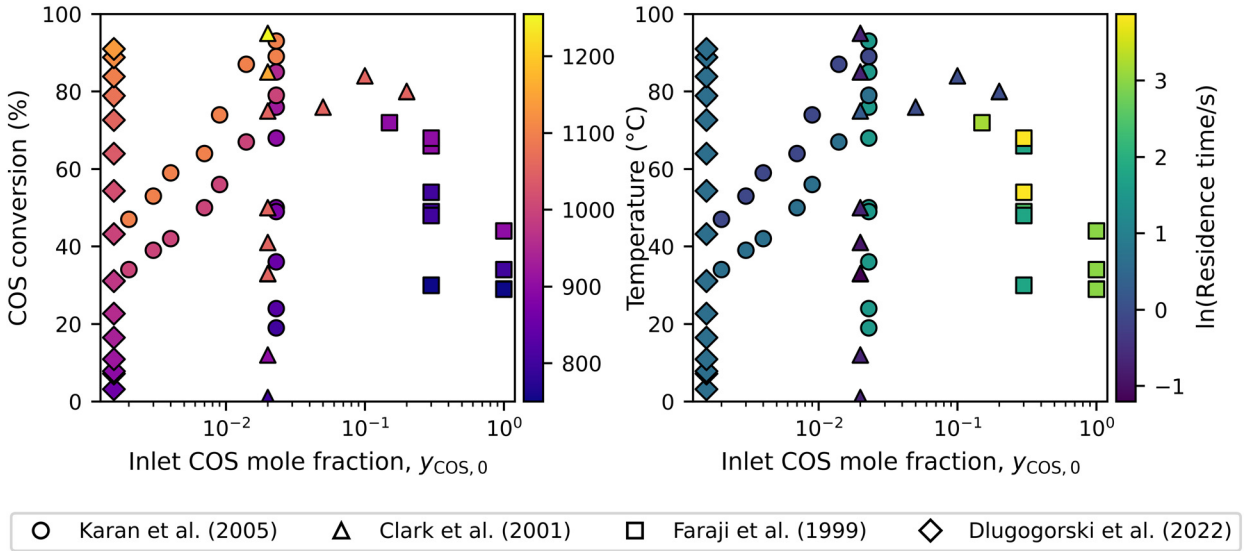

Fig. 1 Overview of the experimental datasets selected for kinetic model development. COS conversion is plotted against inlet COS mole fraction on a logarithmic scale. Marker shape denotes the literature source, while color indicates temperature (left) and ln(residence time/s) (right). The figure summarizes the range of operating conditions and the associated conversion behavior covered by the compiled data.

conditions, consistency with thermodynamic trends, and parameter identifiability from the available experimental observables. As an additional screening step, standard-state equilibrium coefficients were calculated for all candidate reactions over the investigated temperature range using standard Gibbs free energies of formation taken from the NIST-JANAF thermochemical tables.[28] The resulting equilibrium-coefficient analysis, including the corresponding $\log_{10}(K_p)$ plot, is provided in the SI. This analysis was used as a thermodynamic plausibility check and not as a substitute for kinetic validation, since a thermodynamically accessible reaction is not necessarily kinetically relevant under the considered reaction conditions.

The purpose of the reaction selection was therefore not to exclude every pathway that may occur under any condition, but to retain only those reactions whose contribution can be meaningfully determined from the available data. This distinction is important because the selected datasets primarily report COS conversion, whereas detailed and internally consistent product-speciation data for atomic sulfur, sulfur allotropes, CS_2, SO, CS, S_3, CO_2, or solid carbon are either unavailable, incomplete, or not sufficiently systematic for independent kinetic parameter estimation. For several candidate reactions, reliable apparent kinetic data over the investigated temperature and composition range are also unavailable. Consequently, including such pathways would require assuming rate parameters for reactions that cannot be independently regressed by the experimental observables.

Reactions 1–4 were retained in the kinetic network. Reaction 1 represents pressure-dependent unimolecular COS decomposition and was regressed independently using the QRRK formulation described in section 2.3. Reaction 2 represents the concentration-dependent bimolecular COS-consumption pathway and its reverse COS-formation pathway. This reaction is required to reproduce the experimentally observed dependence of COS conversion on inlet COS concentration and product accumulation. Reaction 3 represents sulfur-atom abstraction from COS, while reaction 4 describes the interconversion between atomic sulfur and S_2. These sulfur-mediated steps are chemically relevant because the availability of atomic sulfur affects secondary COS consumption and reverse COS formation.

Reactions 5–9 were not retained as independently parameterized steps. This should not be interpreted as a definitive rejection of these pathways under all possible conditions, however. The equilibrium-coefficient analysis showed that pathways involving direct formation of atomic sulfur, such as reactions 5 and 6, and the CS/SO forming route, reaction 9, are thermodynamically unfavourable over the investigated temperature range. In contrast, reaction 7, leading to CO_2 and CS_2, and reaction 8, involving S_3, cannot be excluded on thermodynamic grounds alone. Their non-inclusion is therefore based primarily on identifiability rather than thermodynamic impossibility.

In particular, reaction 7 would require reliable CO_2 and CS_2 product data to distinguish its contribution from other carbon–sulfur rearrangement pathways. Reaction 8 would require information on higher sulfur species, especially S_3, while reaction 6 would require consistent evidence of CO_2 and solid carbon formation. Such product-resolved data are absent or not sufficiently reliable in the selected reactor datasets. As a result, no reliable apparent kinetics or meaningful sensitivity analysis can be established for these pathways within the present reactor-conversion dataset. Including reactions 5–9 would therefore increase model complexity by introducing uncertain rate parameters, without improving the identifiability of the kinetic model.

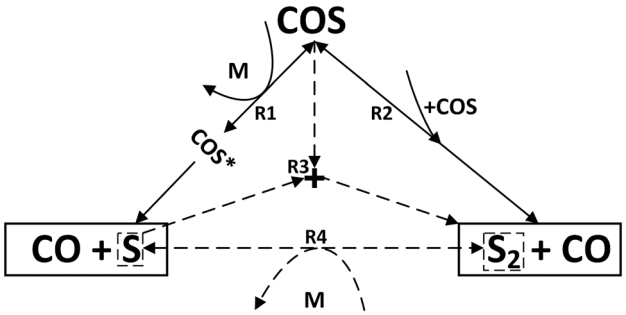

Fig. 2 Conceptual reaction-path scheme for the COS pyrolysis model. Solid arrows denote COS decomposition pathways, whereas dashed arrows denote sulfur-mediated steps involving atomic sulfur or S_2 as reacting or interconverting sulfur species. The scheme is conceptual and is not intended as a fully stoichiometric elementary mechanism.

Based on these considerations, the kinetic framework retained in this work can be summarized by reactions 1–4 and is schematically represented in Fig. 2. The scheme is intended to provide a conceptual representation of the reaction network used for modelling, rather than a fully stoichiometric elementary mechanism. Solid arrows denote COS decomposition pathways, including the pressure-dependent unimolecular route and the bimolecular COS decomposition route. Dashed arrows denote sulfur-mediated steps, *i.e.* reactions in which atomic sulfur or S_2 participate as reacting or interconverting sulfur species. In this representation, R1 describes collisionally activated unimolecular COS decomposition, R2 represents bimolecular COS decomposition and its reverse contribution to COS formation, R3 accounts for sulfur-mediated COS consumption by atomic sulfur, and R4 represents third-body-assisted sulfur interconversion between S and S_2. This schematic therefore highlights how the direct COS decomposition pathways are coupled to the sulfur-species pool in the reaction network.

2.3. Pressure-dependent treatment of unimolecular COS decomposition

A mechanistic description of unimolecular COS decomposition (reaction 1) can be introduced through the RRKM-type mechanism:[36]

$$\mathrm{COS} + \mathrm{M} \leftrightarrow \mathrm{COS}^* + \mathrm{M} \overset{k_{\mathrm{RRKM}}(E)}{\rightarrow} \mathrm{COS}^{\ddagger} \rightarrow \mathrm{CO} + \mathrm{S} \qquad (1)$$

In the first step, collisions with inert third-body molecules (M) produce vibrationally excited COS (denoted as COS*). A limited fraction of these collisions result in sufficient energy transfer to promote the molecule into a vibrationally activated state, representing the fraction of COS + M collisions that successfully generate COS*. In the second step, only a subset of the COS* population will possess the correct distribution of internal energy modes to localize energy along the reaction coordinate and cross the transition state ($COS^{\ddagger}$), ultimately leading to bond rupture and product formation.[25]

A full RRKM/master-equation treatment would describe this process using the energy-dependent microcanonical rate coefficient $k_{\mathrm{RRKM}}(E)$, the density and sum of states, and a model for collisional energy transfer. For COS, such a treatment is further complicated by the fact that formation of CO and ground-state atomic sulfur involves electronic states of different spin multiplicity. A complete description would therefore require information on the relevant singlet and triplet potential-energy surfaces, their crossing region, and the associated non-adiabatic coupling. This level of detail is outside the scope of the present reactor-scale kinetic model. Therefore, the pressure-dependent unimolecular rate coefficient was represented using an effective quantum RRK formulation, which retains the main falloff features while remaining compact enough for kinetic modelling.

The high-pressure-limit rate coefficient was written in Arrhenius form as shown in eqn (2)

$$k_{\infty}(T) = A_1 e^{\left(-\frac{E_0}{RT}\right)} \qquad (2)$$

where A_1 is the high-pressure limit pre-exponential factor, E_0 is the threshold energy for decomposition, R is the gas constant, and T is the temperature. At finite pressure, the effective rate coefficient was calculated by applying a quantum RRK falloff correction to $k_{\infty}(T)$ according to eqn (3).[30]

$$k_1(T,[\mathrm{M}]) = k_{\infty}(T)\left(1-q_{\mathrm{v}}\right)^{s} \sum_{p=0}^{\infty} \frac{q_{\mathrm{v}}{}^{p}\,\frac{(p+s-1)!}{(p!(s-1)!)}}{1+\frac{A_1}{k_{\mathrm{de}}(T)[\mathrm{M}]}\frac{(p+m)!(p+s-1)!}{p!(p+m+s-1)!}} \qquad (3)$$

where s is the number of active vibrational modes, p is the number of excess vibrational quanta above the decomposition threshold, and q_{v} is the vibrational Boltzmann factor described in eqn (4).

$$q_{\mathrm{v}} = e^{\left(-\frac{hc\bar{\nu}}{k_{\mathrm{B}}T}\right)} \qquad (4)$$

Here, h is Planck's constant, c is the speed of light, k_{B} is Boltzmann's constant, and $\bar{\nu}$ is an effective vibrational frequency. In the present QRRK formulation, $\bar{\nu}$ is the only molecular vibrational input required. It was calculated as the geometric mean of the four normal-mode frequencies of linear OCS, including the doubly degenerate bending mode and the two stretching modes, as summarized in Table 2. These frequencies were taken from the computational study of Lara-Cruz and Moyano,[24] who investigated OCS isomerization and dissociation kinetics using statistical kinetic models. In

Table 2 Normal mode frequencies[24]

Species	Frequencies (cm^{-1})			
	ω_1	ω_2	ω_3	ω_4
OCS	524.51	524.51	871.31	2098.32

that work, the molecular structures and vibrational properties were evaluated after comparison of several electronic-structure levels, and CCSD(T)/aug-cc-pVTZ was selected for the main electronic-structure description.

The parameter m represents the decomposition threshold expressed in units of the effective vibrational quanta as shown in eqn (5).

$$m = \frac{E_0}{N_A h c \bar{\nu}} \tag{5}$$

where N_A is Avogadro's number. This definition follows from the standard RRK/QRRK description, in which the molecule is treated as a set of s harmonic oscillators and the internal vibrational energy is expressed as a number of quanta, $E = nhc\bar{\nu}$. In this framework, dissociation requires that a critical amount of energy is localized in the reactive mode; therefore, the threshold energy can be written as $E_0 = mhc\bar{\nu}/N_A$, where m is the critical number of effective vibrational quanta required to reach the decomposition threshold. Since m is not generally an integer, it was treated as a continuous quantity in the QRRK summation. The factorial terms involving non-integer m were evaluated using gamma functions. In eqn (3), p represents the number of excess vibrational quanta above this threshold, so that each term in the summation corresponds to an excitation level of approximately $m + p$ effective vibrational quanta.[29]

The molecular information used in the present QRRK treatment is therefore limited to the normal-mode frequencies required to define $\bar{\nu}$. Unlike a full TST, RRKM, or master-equation calculation, the present formulation does not use transition-state frequencies, moments of inertia, rotational partition functions, or explicitly calculated densities and sums of states. Consequently, the parameters A_1, E_0 and ψ should be interpreted as effective, formulation-dependent falloff parameters obtained by regression against independent pressure-dependent direct-rate data, rather than as unique *ab initio* molecular constants. The uncertainty associated with the fixed vibrational frequencies enters indirectly through q_v and m. Because A_1, E_0 and ψ are optimized against experimental $k_1(T[M])$ data, part of this uncertainty is absorbed into the fitted QRRK parameter set. This limitation is taken into account by using the optimized expression only as a compact pressure-dependent parameterization of reaction 1 in the reactor model.

The collisional deactivation rate coefficient was estimated from gas-kinetic theory as shown in eqn (6)[17]

$$k_{de}(T) = \psi\left(\frac{8k_B T}{\pi\mu}\right)^{0.5} \tag{6}$$

where Ψ is an effective collision cross-sectional area and μ is the reduced mass of the COS–inert pair.

The denominator in eqn (3) describes the competition between unimolecular decomposition and collisional deactivation. The ratio $A_1/k_{de}(T)[M]$ compares the intrinsic unimolecular attempt frequency with the frequency of collisional deactivation. At higher bath-gas concentrations, $k_{de}(T)[M]$ increases, collisional deactivation is more frequent, and the rate coefficient approaches the high-pressure limit. At lower bath-gas concentrations, collisional deactivation is less frequent and the rate coefficient becomes more pressure dependent. The factorial term multiplying this ratio accounts for the probability that the available vibrational energy is distributed in a way that enables decomposition. Therefore, the QRRK summation accounts for both the quantized distribution of vibrational energy and the pressure dependence caused by collisional deactivation.

In the reactor model, the resulting pressure-dependent rate coefficient was used directly as a first-order unimolecular rate coefficient: $r_1 = k_1(T,[M])C_{COS}$. The adjustable parameters in the QRRK formulation were A_1, E_0, and ψ. The number of active vibrational modes was fixed at $s = 2$.[17] This kept the formulation compact while retaining an explicit pressure dependence and a statistical description of vibrational energy quantization. The optimized QRRK expression was then used to describe the pressure-dependent unimolecular COS decomposition step in all subsequent kinetic simulations.

2.4. Reactor model

An isothermal plug flow reactor (PFR) model was selected to maintain consistency with the experimental conditions reported by Clark *et al.*, Karan *et al.* and Faraji *et al.* respectively,[2,10,14] where isothermal operation was explicitly stated. The assumption of ideal plug flow behavior is supported by the high reactor length-to-diameter ratios (23–3200) and the calculated Peclet numbers, which range from 54 to 10^6. These values, calculated at the inlet conditions, indicate that axial dispersion is negligible in comparison to advective flow, with advection overwhelmingly dominating the transport processes.

For the experimental data-set of Dlugogorski, *et al.*,[16] an isothermal continuous stirred tank reactor (CSTR) model was used, as the reactor employed was a jet-stirred reactor (JSR) described by Zeng, *et al.*[31] The JSR exhibits a very low Peclet number ($6–8 \times 10^{-3}$), indicating near-complete mixing and negligible advective flow compared to dispersion, thereby justifying the use of a CSTR model. The diffusion coefficient was assumed to be the molecular diffusivity of the feed, and the binary diffusion coefficients were calculated using the correlation by Fuller *et al.*[32–34]

The PFR employed reactor model, as described by eqn (7), where d_t represents the tube diameter, ε is the porosity, F_i is the species molar flow, and R_{vi} is the species volumetric production rate [mol m^{-3} s^{-1}]. For empty tube experiments,[2,10] ε assumes a value of 1, while for experiments with the inert packing,[14] ε is set at 0.5. The CSTR model is presented in eqn (8), where V is the volume of the reactor

$$\frac{\mathrm{d}F_\mathrm{i}}{\mathrm{d}z} = \varepsilon \frac{\pi {d_\mathrm{t}}^2}{4} R_\mathrm{v,i} \tag{7}$$

$$F_\mathrm{i} = F_\mathrm{i,in} + R_\mathrm{v,i} V \tag{8}$$

2.5. Parameter estimation and statistical analysis

Parameter estimation was performed sequentially. In the first step, the parameters of the pressure-dependent QRRK formulation for the unimolecular decomposition rate coefficient $k_1(T,[\mathrm{M}])$ were estimated by minimizing the sum of squared residuals between experimental and modelled $k_1(T,[\mathrm{M}])$ values. Since the available unimolecular rate-coefficient data span several orders of magnitude, the regression was performed using logarithmic residuals. The objective function for the $k_1(T,[\mathrm{M}])$ regression was expressed as shown in eqn (9).

$$\mathrm{SSQ}_{\mathrm{res},k_1} = \sum_{j=1}^{n} \left[\log_{10}\left(k_{1,j}\right) - \log_{10}\left(\hat{k}_{1,j}\right) \right]^2 \rightarrow \mathrm{Min} \tag{9}$$

where $k_{1,j}$ represents the experimental pressure-dependent unimolecular rate coefficient and $\hat{k}_{1,i}$ is the corresponding value calculated using the QRRK formulation. This first regression provided the optimized QRRK parameters A_1, E_0, and ψ, which were then kept fixed in the subsequent reactor-model regression.

In the second step, the remaining kinetic parameters were estimated by minimizing the sum of squared residuals between the experimental COS conversion data and the model predictions. Specifically, the conversion residuals were calculated as the difference between the observed COS conversion values and the simulated ones. The objective function for the reactor-model regression was expressed as:

$$\mathrm{SSQ}_{\mathrm{res},X} = \sum_{j=1}^{n} \left(X_{\mathrm{COS},j} - \hat{X}_{\mathrm{COS},j}\right)^2 \rightarrow \mathrm{Min} \tag{10}$$

where $X_{\mathrm{COS},j}$ represents the experimental COS conversion data points, and $\hat{X}_{\mathrm{COS},j}$ the corresponding model simulated values. This minimization approach ensures that the model parameters are adjusted such that the difference between the observed and model simulated COS conversion is minimized across all experimental data points.

For the tubular-reactor datasets, the reactor model was solved using SciPy's solve_ivp routine with the backward differentiation formula (BDF) method. For the JSR dataset, the steady-state CSTR equations were solved using SciPy's fsolve routine. Parameter estimation was then carried out using SciPy's least_squares function. Parameter bounds were imposed where required to ensure physically meaningful values.

The statistical significance of the estimated parameters was evaluated from their associated t values, calculated as the ratio of the parameter estimate to its standard error.[35] In addition to statistical significance, the estimated parameters were assessed for physical plausibility. The overall significance of the regression was evaluated using the F test:

$$F_\mathrm{c} = \frac{\frac{\mathrm{SSQ}_\mathrm{reg}}{p}}{\frac{\mathrm{SSQ}_\mathrm{res}}{n-p-1}} \tag{11}$$

where p is the number of estimated parameters and n is the number of data points. The regression sum of squares was calculated as:

$$\mathrm{SSQ}_\mathrm{reg} = \sum_{j=1}^{n} \left(\hat{y}_j - \overline{y}\right)^2 \tag{12}$$

where y represents the dependent variable used in the corresponding regression. For the k_1 regression, $y = \log_{10}(k_1)$, whereas for the reactor-model regression, $y = X_\mathrm{COS}$. The goodness of fit was further assessed using the coefficient of determination, R^2. For the k_1 regression, R^2 was evaluated on the logarithmic rate-coefficient values, while for the reactor-model regression it was evaluated using the COS conversion values. Because replicated experimental points were not available, formal lack-of-fit testing was not possible; instead, model adequacy was examined qualitatively through residual analysis, with particular attention to the absence of systematic trends.

Results and discussion

3.1. Assessment of the QRRK formulation for unimolecular COS decomposition

Before optimizing the full kinetic model against the reactor conversion data, the unimolecular decomposition step was assessed separately. This was done in two stages. First, the pressure-dependent QRRK formulation for reaction 1 was regressed against independent direct-rate data from the literature. Second, the optimized $k_1(T,[\mathrm{M}])$ expression was implemented as the only COS-consuming reaction in the PFR and CSTR reactor models to evaluate whether unimolecular decomposition alone could account for the observed COS conversions.

The direct-rate dataset used for this regression was compiled from three literature sources reporting COS thermal decomposition under shock-tube conditions. The dataset includes the recent measurements of Panda *et al.* 2026,[17] who reported pressure-dependent rate coefficients for OCS decomposition in different bath gases using laser absorption spectroscopy; the high-temperature shock-tube data of Hay and Belford, 1967 (ref. 8) obtained using quadrupole mass spectrometry; and the earlier shock-wave measurements of Schecker and Wagner, 1969 (ref. 7) for COS decomposition in argon. These datasets were selected because they provide direct information on the unimolecular decomposition rate over a broad range of temperatures, pressures, and bath-gas concentrations, making them suitable for regressing the pressure-dependent QRRK formulation independently from the

Table 3 Optimized parameters and regression statistics for the QRRK formulation of unimolecular COS decomposition

Parameter	Value	t Value[a]
A_1 (s^{-1})	$(4.53 \pm 1.37) \times 10^{10}$	3.30
E_0	243.53 ± 4.21	57.78
Ψ (m^2)	$(9.03 \pm 1.94) \times 10^{-21}$	4.65
s^b	2	—
$\bar{\nu}$ $(cm^{-1})^b$	841.91	—
m^b	24.18	—

[a] Tabulated t value: 1.98. [b] Fixed or calculated parameter; not included as an adjustable regression parameter.

reactor conversion data. The individual data points, including temperature, pressure or bath-gas concentration, bath gas, reported rate coefficient, and converted quantities used in the regression, are provided in the SI.

The optimized QRRK parameters and statistical indicators are summarized in Table 3. The fitted parameters were statistically significant, with calculated t values larger than the tabulated value at the 95% confidence level. An F value of 576 and the log-scale R^2 of 93.7% indicate that the QRRK formulation explains most of the variability in the compiled direct-rate data and that the model is globally significant.

The optimized QRRK parameters can be compared most directly with the RRK parameters reported by Panda *et al.*,[17] since both formulations describe the pressure-dependent unimolecular decomposition rate using a falloff expression that includes a frequency factor, a critical energy, an effective number of oscillators, and a collisional deactivation term. Panda *et al.*[17] reported s = 2, E_0 of 283 kJ mol^{-1}, A_1 of 4.99×10^{11} s^{-1} and ψ of 6.95×10^{-20} m^2. In the present work, the optimized QRRK expression gives lower values of A_1, E_0, and ψ. This difference is expected because the present regression was performed over a combined dataset including Panda *et al.*,[17] Hay and Belford,[8] and Schecker and Wagner[7] rather than only the Panda dataset. In addition, the present formulation uses the quantum RRK summation rather than the classical Kassel integral, so the fitted parameters should be interpreted as formulation-dependent effective parameters rather than direct one-to-one replacements of the classical RRK values.

The activation-energy scale obtained here is also consistent with the older shock-tube studies, although the comparison is less direct. Hay and Belford reported a low-pressure unimolecular expression with an apparent critical activation energy of 299 kJ mol^{-1}, while Schecker and Wagner reported apparent low- and high-pressure activation energies of approximately 255 and 285 kJ mol^{-1}. The QRRK-fitted E_0 obtained in the present work lies somewhat below these apparent values, but remains in the same order of magnitude. This is reasonable because E_0 in the QRRK formulation is not a simple Arrhenius activation energy; it is optimized together with A_1 and ψ to reproduce the pressure-dependent falloff behavior across multiple datasets. Therefore, differences between the fitted QRRK threshold energy and the apparent activation energies reported in earlier Arrhenius-type analyses should not be interpreted as a contradiction. The pressure dependence predicted by the optimized QRRK formulation is shown in Fig. 3 for 1870 and 2380 K, together with literature data. The model reproduces the expected falloff behaviour of a pressure-dependent unimolecular reaction. At low bath-gas concentration, $k_1(T,[M])$ increases strongly with [M], whereas at higher [M] the sensitivity to concentration decreases and the rate gradually approaches the high-pressure limit. The agreement with the experimental points is satisfactory at both temperatures, indicating that the optimized QRRK formulation captures the main pressure dependence of the unimolecular COS decomposition step.

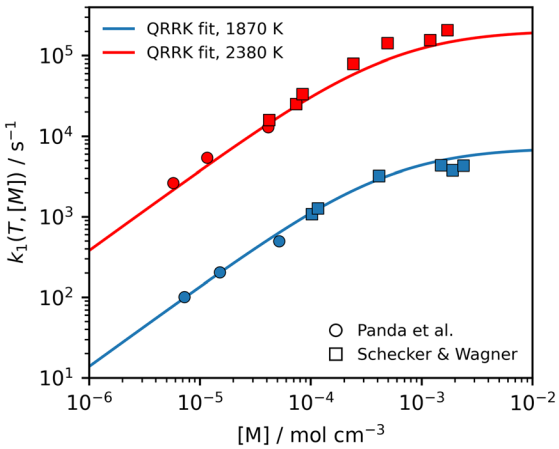

Fig. 3 Pressure dependence of the optimized QRRK formulation for COS unimolecular decomposition.

The overall agreement between the QRRK model and the compiled direct-rate dataset is shown in the parity diagram

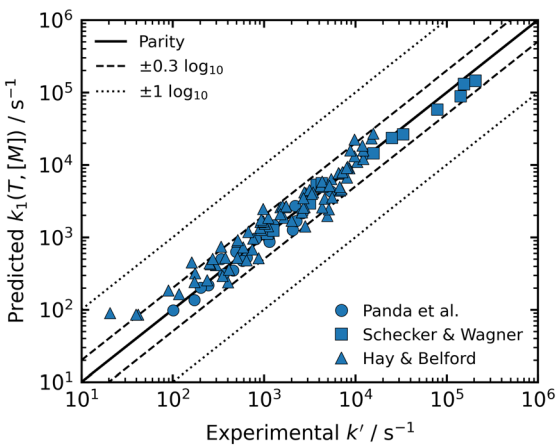

Fig. 4 Parity diagram for the optimized QRRK formulation applied to the direct COS decomposition rate dataset. Experimental pseudo-first-order rate coefficients, k'_1, are compared with QRRK-predicted $k_1(T,[M])$.

in Fig. 4. The optimized expression reproduces the different literature datasets with reasonable consistency over several orders of magnitude in $k_1(T,[M])$. Most points lie close to the parity line, with the majority of the data falling within the ±1 $\log_{10}$ band and nearly all points remaining within the ±0.3 $\log_{10}$ band. This confirms that the fitted QRRK expression provides a satisfactory global description of the available direct-rate data.

The classical RRK formulation was also examined for comparison. When optimized independently, the classical and quantum forms yielded similar overall goodness of fit for the direct-rate dataset. However, when evaluated at the lower-temperature conditions relevant to the PFR and CSTR datasets, the classical RRK expression systematically predicted somewhat higher $k_1(T,[M])$ values than the QRRK expression, typically by approximately 5–10%. This difference is consistent with the physical basis of the two approaches. The classical RRK formulation treats the internal vibrational energy distribution as continuous, whereas the QRRK formulation retains the quantized character of vibrational energy. At the lower temperatures relevant to the reactor datasets, fewer high-energy vibrational states are populated, making the quantum description more restrictive. Since both formulations described the direct-rate data comparably well, the QRRK form was selected for the remainder of this work as the more suitable representation of the pressure-dependent unimolecular decomposition step.

After the independent regression of $k_1(T,[M])$, the optimized QRRK expression was implemented as the sole COS-consuming reaction in the reactor model. The resulting parity diagram is shown in Fig. 5. Although the QRRK formulation satisfactorily reproduces the direct-rate data, the unimolecular-only model systematically underpredicts COS conversion in both the PFR and CSTR datasets. This underprediction is especially clear at intermediate and high experimental conversions, where the predicted conversion remains well below the parity line. Therefore, the discrepancy cannot be attributed only to the pressure-dependent formulation of $k_1(T,[M])$, but indicates that unimolecular COS decomposition alone is insufficient to describe the reactor conversion data.

This result motivated the inclusion and regression of additional sulfur-forming reaction pathways in the full kinetic model, while keeping the QRRK-derived $k_1(T,[M])$ parameters fixed. In this way, reaction 1 remains constrained by independent pressure-dependent rate-coefficient data, and the reactor conversion data are used to estimate only the remaining kinetic parameters.

3.2. Assessment of the literature-parameterized reaction network

After demonstrating that the optimized QRRK unimolecular decomposition step alone could not reproduce the reactor-conversion data, the retained reaction network was evaluated using literature parameters for the remaining reactions. This simulation was performed without regression to the reactor-conversion data. Reaction 1 was represented by the independently fitted QRRK expression, while reactions 2–4 were included using literature-reported Arrhenius or modified Arrhenius parameters summarized in Table 1.

Several literature-parameter combinations were evaluated, reflecting the available parameterizations for both the bimolecular COS-consumption pathway, reaction 2, and the sulfur-abstraction pathway, reaction 3. Reaction 4, describing S_2/S_1 interconversion, was retained using fixed literature parameters because sulfur allotrope concentrations were not measured in any of the selected reactor datasets. Among the literature-only combinations tested, the best-performing case was obtained using A_{2f} = 4.39 × 10^9 m^3 mol^{-1} s^{-1} and Ea_{2f} = 197 kJ mol^{-1} for the forward direction of reaction 2, A_{2r} = 318 m^6 mol^{-2} s^{-1} and Ea_{2r} = 56 kJ mol^{-1} for the reverse direction of reaction 2, and A_3 = 2.2 × 10^6 m^3 mol^{-1} s^{-1} and Ea_3 = 34.8 kJ mol^{-1} for reaction 3.

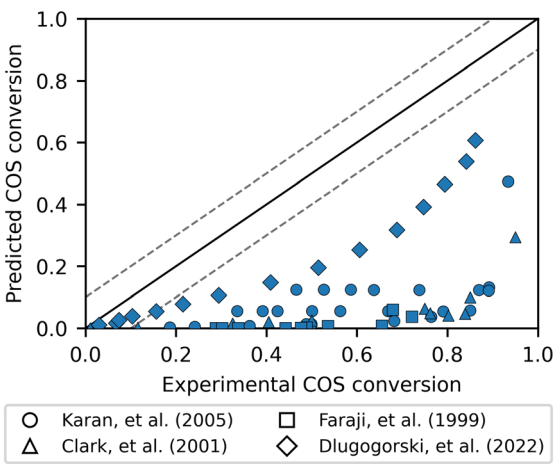

Fig. 5 QRRK reaction-1-only parity diagram for COS conversion.

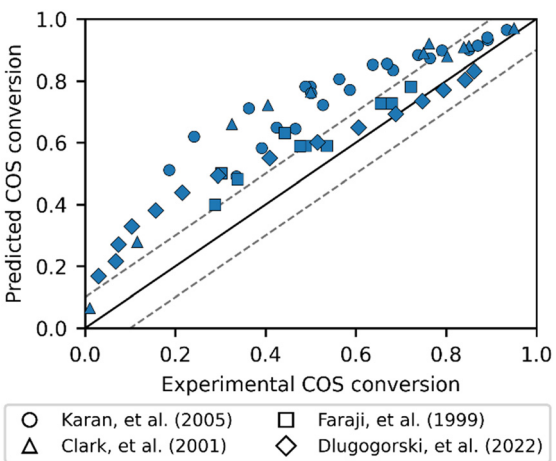

Fig. 6 Parity diagram for the retained COS pyrolysis network using the best-performing literature-only parameter combination.

The corresponding parity diagram is shown in Fig. 6. Although inclusion of the literature-based secondary reactions improved the description compared with the reaction-1-only model (Fig. 5), the agreement remained insufficient over the full dataset. The literature-parameterized network systematically overpredicted COS conversion, as indicated by the negative mean residual of −0.145. The resulting R^2 was only 53.1%.Thus, even the best direct consolidation of literature parameters could not provide a satisfactory unified description of the selected PFR and CSTR datasets.

This result indicates that the retained reaction network is chemically necessary, but that the available literature parameters cannot be transferred directly and simultaneously across the broad range of reactor types, temperatures, residence times, and COS feed compositions considered here.

Although reactions 3 and 4 were retained, their kinetic parameters were not independently estimated in this work. Reaction 3 depends directly on the concentration of atomic sulfur, which was not measured in the selected reactor datasets and is itself generated and redistributed through reactions 1 and 4. Similarly, reaction 4 controls the distribution between atomic sulfur and S_2, but the selected datasets do not distinguish between these sulfur species or higher sulfur allotropes. Fitting these parameters using COS conversion data alone would therefore introduce strong compensation between the predicted sulfur pool and the sulfur-mediated reaction rates. Reactions 3 and 4 were therefore included using literature kinetic parameters. The systematic deviations justify targeted re-estimation of the identifiable parameters. The subsequent regression was therefore restricted to the forward and reverse parameters of reaction 2, whose contributions are directly reflected in the observed dependence of COS conversion on feed concentration and product accumulation.

3.3. Optimization of the bimolecular COS pyrolysis kinetic parameters

Following the assessment of the unimolecular-only and literature-parameterized reaction networks, the final regression was restricted to the reversible bimolecular COS decomposition pathway, reaction 2. The pressure-dependent unimolecular decomposition rate coefficient $k_1(T,[\mathrm{M}])$ was kept fixed using the QRRK formulation obtained from direct rate-coefficient data, as described in section 3.1. The parameters of the sulfur-abstraction pathway, reaction 3, and the sulfur interconversion pathway, reaction 4, were also fixed to literature values, as justified in section 3.2. Therefore, only the forward and reverse Arrhenius parameters of reaction 2 were treated as adjustable.

Table 4 Knockout analysis

Case	SSR	R^2
Full model	0.093	97.5
No. R3	0.180	95.0
No. R1	0.458	86.9
No. R4	1.167	69.2
No. $R2_r$	1.292	65.9
No. $R2_f$	11.020	−190.7
No. R2	14.152	−273.3

The parameters A_{2f}, Ea_{2f}, A_{2r} and Ea_{2r} were estimated simultaneously using the complete COS conversion dataset, including both dilute and concentrated COS feeds. This approach avoids imposing a composition threshold during the final regression while allowing the reverse direction of reaction 2 to be informed by the high-COS and high-conversion experiments, where CO and sulfur-containing products accumulate.

The nonlinear regression provided a strong description of the full dataset, with an R^2 of 97.5%. The global F value of 555 was well above the critical value of 2.54, confirming the statistical significance of the regression. The optimized parameters are reported in Table 5.

As a diagnostic test, the model was first evaluated with the reverse direction of reaction 2 disabled. This simulation was not used as the final parameter regression, but served to determine whether the COS-consuming pathways alone were sufficient across the full composition range. As shown in Fig. 8(a), the model reproduced most experiments with inlet COS mole fractions below 10%, but systematically overpredicted conversion for experiments with inlet COS mole fractions of 10% or higher. This behaviour indicates that, under concentrated-feed conditions, COS consumption by reaction 1 and reaction 2 forward alone is insufficient to describe the observed conversion. The overprediction is consistent with the increasing relevance of reverse COS formation as CO and sulfur-containing products accumulate along the reactor. Therefore, the reverse direction of reaction 2 was retained in the final simultaneous regression over the complete dataset.

Reaction 1 is required to represent the pressure-dependent unimolecular decomposition of COS, while reaction 2 forward provides the main concentration-dependent COS-consuming pathway. The stronger contribution of reaction 2 is mechanistically consistent with its quadratic dependence on COS concentration. Reactions 3 and 4 are retained to preserve the sulfur-mediated reaction structure, but their parameters are not independently optimized because their individual effects cannot be robustly identified from COS conversion data alone in the absence of sulfur-speciation measurements.

Beyond confirming their statistical importance, the model also provides insight into the relative mechanistic roles of reactions 1 and 2 across the investigated operating window. Their competition can be interpreted directly from the structure of the rate expressions. reaction 1 is first order in COS, with a pressure-dependent rate coefficient $k_1(T,[\mathrm{M}])$ that depends on the effective bath-gas concentration through the

Table 5 Proposed kinetic model for COS pyrolysis

#	Reaction	Rate expression	Parameter	Value	t value[a]	Ref.
1	COS + M → CO + S + M	$r_1 = k_1(T,[M])C_{COS}$	$\bar{\nu}$ (cm^{-1})[b]	841.91	—	This work
			m[b]	24.18	—	This work
			Ψ (m^2)	(9.03 ± 1.04) × 10^{-21}	4.65	This work
			A_1 (s^{-1})	(4.53 ± 1.37) × 10^{10}	3.30	This work
			E_0 (kJ mol^{-1})	243 ± 4.21	57.78	This work
2	COS + COS ⇌ 2CO + S_2	$r_{2f} = k_{2f}C_{COS}^2$	A_{2f} (m^3 mol^{-1} s^{-1})	(9.9 ± 0.4) × 10^9	48.94	This work
			Ea_{2f} (kJ mol^{-1})	218 ± 11	44.68	This work
		$r_{2r} = k_{2r}C_{CO}^2C_{S_2}$	A_{2r} (m^6 mol^{-2} s^{-1})	3166 ± 1606	3.95	This work
			Ea_2r (kJ mol^{-1})	82 ± 39	4.22	This work
3	COS + S → CO + S_2	$r_3 = k_3C_{COS}C_S$	A_3 (m^3 mol^{-1} s^{-1})	2.2 × 10^6	—	16
			Ea_3 (kJ mol^{-1})	34.8	—	16
4	S_2 + M ⇌ 2S + M	$r_{4f} = k_{4f}C_{S_2}C_M$	A_{4f} (m^3 mol^{-1} s^{-1})	3 × 10^9 (m^3 mol^{-1} s^{-1})	—	18, 19
			Ea_{4f} (kJ mol^{-1})	425		
		$r_{4r} = k_{4r}C_S^2$	A_{4r} (m^3 mol^{-1} s^{-1})	5.5 × 10^4 (m^3 mol^{-1} s^{-1})	—	18
			Ea_{4r} (kJ mol^{-1})	3.45		

[a] Tabulated t value: 2.003. [b] Calculated *via* theoretical methods. $k_1(T,[M])$ is estimated based on eqn (3). k_{2f} was estimated based on the low-concentration datasets, whereas k_{2r} was derived from the high-concentration datasets.

QRRK falloff formulation. By contrast, the forward direction of reaction 2 is second order in COS. Therefore, the relative importance of reaction 2 increases with increasing COS concentration and decreasing dilution, while reaction 1 becomes more competitive at higher temperature and with greater collisional activation through the bath gas.

To further assess the relative importance of the retained reaction pathways in the final model, a knockout analysis was performed using the optimized reversible kinetic model over the complete COS conversion dataset. Each reaction contribution was suppressed individually while retaining the optimized or fixed values of the remaining parameters, and the resulting SSR and R^2 were recalculated. As shown in Table 4, removal of the forward direction of reaction 2, caused the largest deterioration in model performance, increasing the SSR from 0.093 to 11.020 and reducing R^2 from 97.5% to −190.7%. Suppression of both the forward and reverse directions of reaction 2 led to an even larger deterioration, with an SSR of 14.152 and an R^2 of −273.3%. This confirms that the bimolecular COS decomposition pathway is the dominant concentration-dependent contribution required to reproduce the COS conversion data.

Removal of the reverse direction of reaction 2 also significantly worsened the model performance, increasing the SSR to 1.292 and reducing R^2 to 65.9%. This supports the inclusion of reverse COS formation in the final reversible model, particularly for concentrated-feed conditions where CO and sulfur-containing products accumulate (Fig. 8(a)). Suppression of reaction 4 also caused a substantial deterioration in the fit, with an SSR of 1.167 and an R^2 of 69.2%. Although reaction 4 does not directly consume or form COS, it controls the redistribution of sulfur between atomic sulfur and S_2. This affects the availability of S_2, which enters directly into the reverse rate of reaction 2. Removing reaction 4 therefore perturbs the sulfur pool and can artificially suppress reverse COS formation, leading to excessive predicted COS conversion under conditions where CO and sulfur-containing products accumulate. Removal of reaction 1 produced a moderate deterioration, confirming that pressure-dependent unimolecular COS decomposition remains an important initiation pathway. In contrast, removal of reaction 3 caused only a smaller increase in SSR, indicating that its individual contribution is less directly identifiable from COS conversion data alone.

This behaviour is illustrated in Fig. 7, which shows the relative contributions of reaction 1 and the forward direction of reaction 2 to direct COS consumption, normalized as R1/(R1 + R2$_f$) and R2$_f$/(R1 + R2$_f$). The reverse direction of reaction 2 is not included in this normalization because it represents COS formation rather than COS consumption. At lower temperatures, reaction 2 forward dominates the simulated COS consumption, consistent with its second-order dependence on COS concentration. As temperature increases, the contribution of reaction 1 becomes

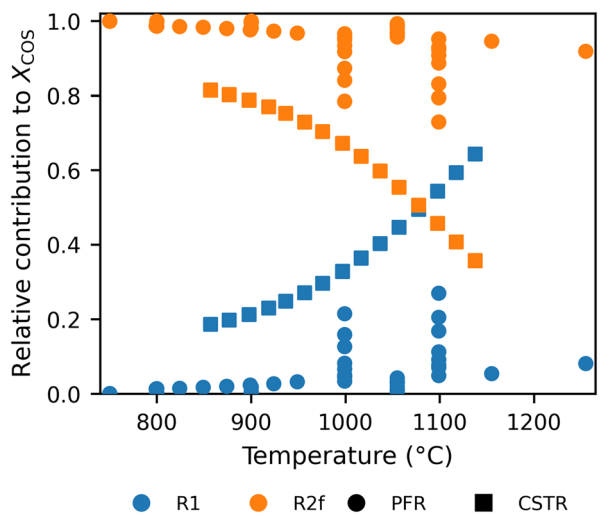

Fig. 7 Relative contributions of reaction 1 and reaction 2 forward to COS consumption.

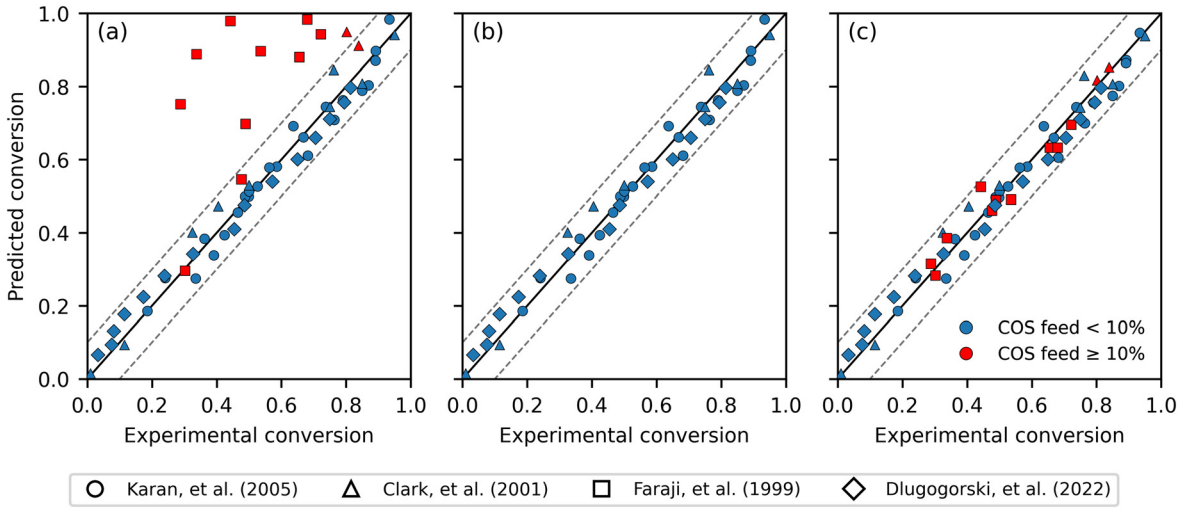

Fig. 8 Parity diagrams for COS conversion at different stages of the model development: (a) global fit excluding the reverse COS-formation pathway, (b) low-COS subset, and (c) final kinetic model including all of the data and reactions. Blue symbols denote experiments with inlet COS concentrations below 10%, and red symbols denote experiments with inlet COS concentrations of 10% or higher. Marker shape identifies the literature dataset.

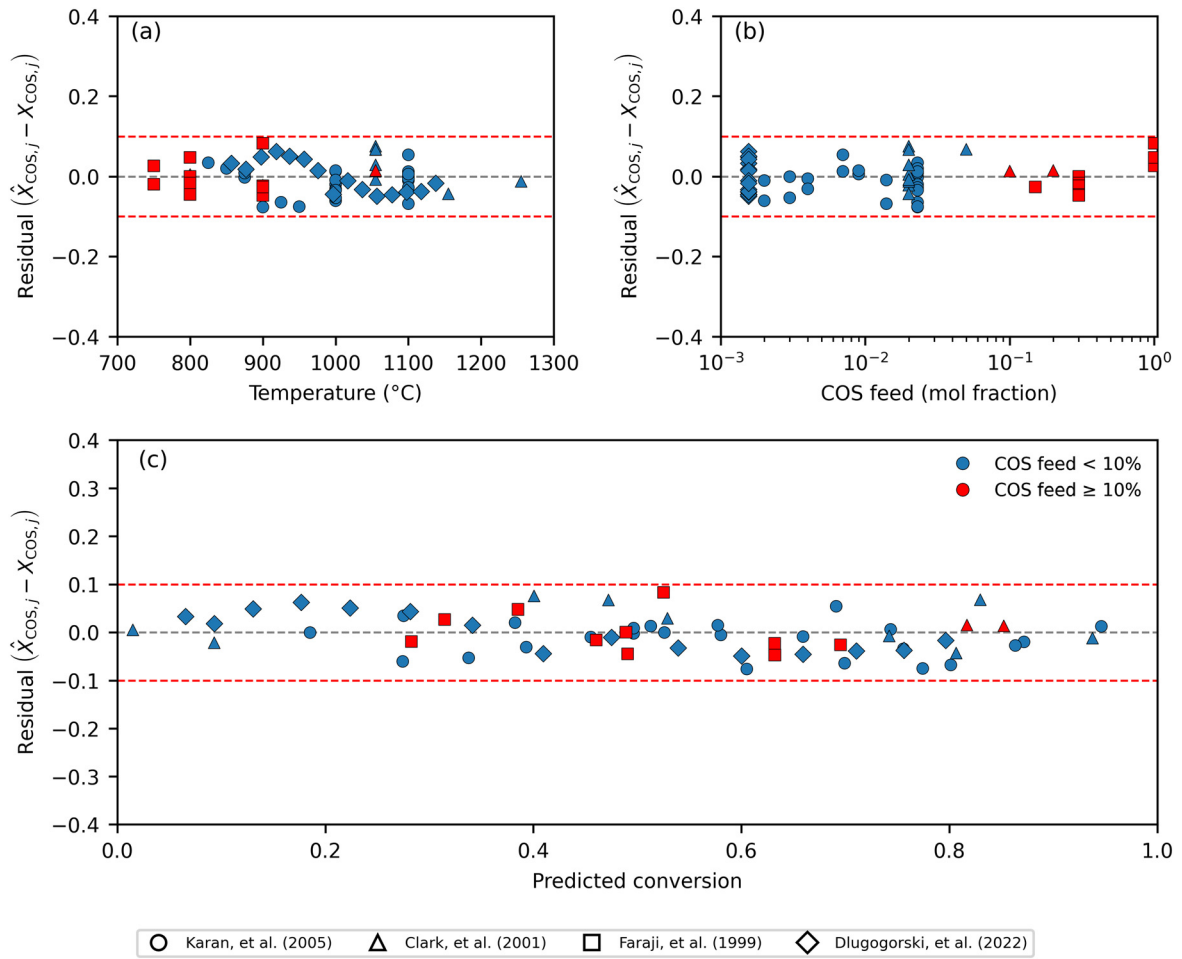

Fig. 9 Residual figures for COS conversion based on the final set of optimized kinetic parameters: (a) residuals as a function of reaction temperature, (b) residuals as a function of initial COS feed composition, shown on a logarithmic scale, and (c) residuals as a function of predicted COS conversion. Blue symbols denote experiments with inlet COS concentrations below 10%, and red symbols denote experiments with inlet COS concentrations of 10% or higher. Dashed red lines indicate residual bounds of ±0.1, and the gray dashed line denotes zero residual.

progressively larger, reflecting the increasing importance of pressure-dependent unimolecular COS decomposition. The figure therefore indicates a gradual transition from a regime dominated by bimolecular COS consumption toward one in which unimolecular decomposition becomes increasingly competitive.

Reaction 3 can also contribute to COS consumption when atomic sulfur accumulates, but its effect depends on the internally generated sulfur pool, which is not directly measured in the available datasets. Similarly, reaction 4 remains mechanistically relevant because it controls the redistribution between S and S_2, thereby affecting both sulfur-mediated COS consumption and reverse COS formation. However, because these sulfur-species concentrations are not independently distinguished by the experimental data, the parameters of reactions 3 and 4 were retained from literature rather than independently optimized.

Fig. 8(b) further supports this interpretation by isolating the experiments with inlet COS mole fractions below 10%, where reverse COS formation is expected to be limited. In this subset, the reverse-disabled model provides good agreement, with the data falling within the ±0.1 deviation band. This confirms that the forward COS-consuming pathways are adequately described under dilute-feed conditions, and that the main limitation of the reverse-disabled model arises when concentrated feeds allow CO and sulfur-containing products to accumulate.

The final simultaneous regression, shown in Fig. 8(c), therefore includes both the forward and reverse directions of reaction 2 and was performed over the complete dataset. The optimized parameters are reported in Table 5. The forward parameters, A_{2f} and Ea_{2f}, are strongly identified, with t values well above the 95% critical value. The reverse parameters, A_{2r} and Ea_{2r}, show broader uncertainty, as expected because reverse COS formation is mainly expressed under concentrated-feed and high-conversion conditions, but both remain statistically significant.

Alternative rate-law formulations for reaction 2 were also tested to verify that the selected expression was not arbitrary. Replacing the forward rate by the mixed-order form $r_{2f} = k_{2f}C_{COS}{}^{1.5}C_M{}^{0.5}$ (ref. 10) substantially worsened the fit, giving an R^2 of 77.7%. Retaining the standard forward expression but using a first-order dependence on CO for the reverse direction, $r_{2r} = k_{2r}C_{CO}C_{S_2}$ improved the fit relative to the mixed-order case but remained inferior to the selected formulation, with an R^2 of 94.9% and in this case, the reverse parameters were not statistically significant. Applying both alternative expressions simultaneously also resulted in poorer performance, with an R^2 of 77.5%. These comparisons support the selected rate expressions shown in Table 5, as the most reliable reversible bimolecular formulation among those tested.

Fig. 9, presents the residual figures for COS conversion as a function of two key independent variables: reaction temperature (a) and initial COS feed composition (b) based on the final set of optimized parameters. In both figures, the residuals remain largely confined within a narrow horizontal band around zero. Although the Dlugogorski, *et al.*[16] dataset shows a slight evolution with temperature, this trend remains within the overall residual spread of the full dataset and does not point to a major systematic bias. This suggests that the model does not systematically over or underpredict COS conversion at specific temperatures or feed compositions, supporting the assumption of homoscedasticity and confirming the model's validity across the full experimental domain.

To further assess the statistical quality of the kinetic model, the residuals were examined relative to the model predictions. Ideally, residuals should be distributed randomly about zero, without a clear dependence on the magnitude of the predicted values. Fig. 9(c) presents the residuals as a function of predicted COS conversion. The distribution is approximately symmetric about zero, with all points remaining within a ±0.1 residual band. No evident funneling or pronounced curvature is observed, suggesting that the model does not exhibit major nonlinearity or heteroscedasticity over the investigated range. Taken together, the residual figures in Fig. 9 support the statistical quality of the proposed kinetic model. The absence of pronounced systematic structure with respect to temperature, feed composition, and predicted conversion suggests that the selected rate expressions and fitted parameters provide a consistent description of the experimental data. This interpretation is further supported by the normal probability plot shown in Fig. 10, which follows an approximately linear trend over most of the range, although some deviation is visible in the tails. Within the investigated operating window, the model can therefore be regarded as statistically robust for predictive purposes.

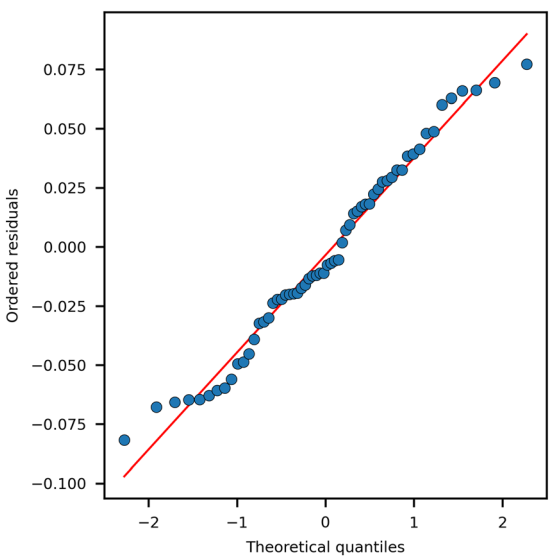

Fig. 10 Normal probability plot of the final model.

3.4. Parameter-propagated uncertainty of the final kinetic model

To assess the robustness of the final kinetic model with respect to uncertainty in the optimized kinetic parameters, a Monte Carlo parameter-propagation analysis was performed. The analysis included the fitted parameters of the QRRK expression for reaction 1 and the Arrhenius parameters of reaction 2 in both the forward and reverse directions. Sampling was performed in the fitted parameter space, using logarithmic variables for the pre-exponential factors and for ψ. This ensured that the corresponding physical parameters remained positive after back-transformation. The optimized values were used as the mean parameter vector, and the covariance matrix was constructed from the standard errors and correlation matrices obtained during the individual regression steps. In this way, the strong correlations between pre-exponential factors and activation energies were retained during sampling. These correlations are important because Arrhenius-type parameters can compensate each other, meaning that relatively large variations in A and $E_{a/0}$ do not necessarily produce equally large variations in the rate coefficient over the fitted temperature range.

For each sampled parameter set, the complete reactor model was solved for all experimental conditions. In total, 2000 independent kinetic-parameter combinations were generated and evaluated, and for each combination the reactor model was solved for every experimental condition. This generated a distribution of predicted COS conversions for every experimental point. The median of this distribution was taken as the central prediction, while the 2.5th and 97.5th percentiles were used to define the 95% parameter-propagated uncertainty interval. To avoid underestimating the uncertainty due to the sequential nature of the fitting procedure, the parameter standard errors were conservatively increased by 5% before sampling. Further details of the covariance construction and sampling procedure are provided in the SI.

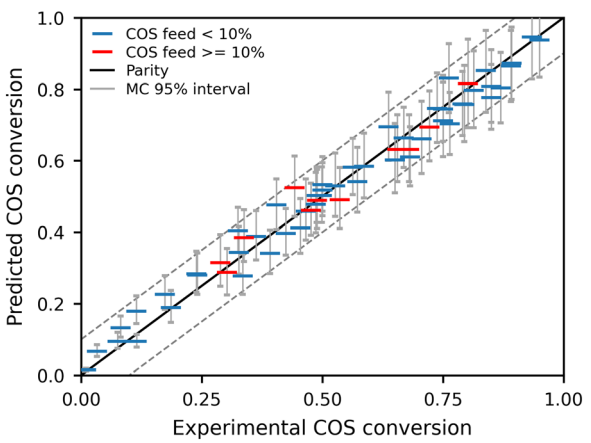

Fig. 11 Monte Carlo parameter-propagated uncertainty intervals for the final kinetic model.

The resulting uncertainty intervals are shown in Fig. 11. The horizontal coloured dashes indicate the median predicted COS conversion, while the vertical grey bars represent the 95% Monte Carlo interval. The uncertainty bands are generally narrow and remain mostly within or near the ±0.1 absolute conversion band. This indicates that, within the investigated temperature, pressure, and composition range, the final model predictions are not highly sensitive to the remaining statistical uncertainty in the fitted kinetic parameters. Even after the conservative 5% increase in parameter uncertainty, the propagated uncertainty in conversion remains modest.

The result is important because it separates parameter uncertainty from other sources of model deviation. The remaining scatter around parity is larger than the Monte Carlo intervals for several points, indicating that these deviations are unlikely to be caused primarily by poor statistical precision of the optimized kinetic parameters. Instead, they more likely reflect experimental scatter, dataset-to-dataset variability, reactor-model idealizations, fixed literature parameters for the sulfur-mediated reactions, and structural limitations of the kinetic mechanism.

It should be emphasized that the intervals shown in Fig. 11 are not full prediction intervals. They only represent the effect of uncertainty in the fitted kinetic parameters of reaction 1 and reaction 2. Uncertainties in temperature, pressure, residence time, inlet composition, reactor geometry, fixed literature rate constants, and model structure were not included. Therefore, the Monte Carlo intervals should be interpreted as parameter-propagated uncertainty bands rather than as total model uncertainty bounds. Within this interpretation, the analysis supports the statistical stability of the final parameter set over the operating window covered by the experimental data.

4. Conclusions

This work demonstrates that COS pyrolysis can be described using a compact reactor-scale kinetic model that remains predictive over the temperature, pressure, and feed-composition ranges covered by the available literature data. By reconciling multiple independent datasets within a single reaction framework, the present study provides a unified kinetic description of COS conversion across both dilute and concentrated regimes. Rather than increasing empirical complexity, the analysis identifies the reaction pathways that are required to reproduce the experimentally observed COS conversion trends.

A central outcome is that the dominant identifiable behaviour of COS pyrolysis is captured by the combination of pressure-dependent unimolecular decomposition and reversible bimolecular COS decomposition. The unimolecular contribution was described using a QRRK-based falloff formulation obtained independently from direct rate-coefficient data. The forward and reverse directions of the bimolecular pathway were then estimated

simultaneously from the complete COS conversion dataset, while the sulfur-mediated reactions were retained using literature parameters. This strategy avoids treating all reactions as freely adjustable empirical terms while preserving a physically interpretable model structure.

The analysis also clarifies the changing roles of the main pathways across the investigated operating window. The forward bimolecular COS-consumption pathway is particularly important when COS availability is high, reflecting its second-order dependence on COS concentration. The unimolecular pathway becomes increasingly competitive at higher temperatures and as COS is depleted. The reverse COS-formation pathway becomes relevant mainly under concentrated-feed and high-conversion conditions, where CO and sulfur-containing products accumulate. Reaction 4, although not directly consuming or forming COS, was found to play an important indirect role by controlling the redistribution between atomic sulfur and S_2. This affects the availability of S_2, which enters directly into the reverse direction of reaction 2, and therefore influences the predicted conversion under concentrated-feed conditions. Nevertheless, because sulfur-species concentrations were not independently measured, the parameters of reaction 4 cannot be robustly identified from COS conversion data alone and were therefore retained from literature values rather than independently optimized.

Monte Carlo propagation of the fitted-parameter covariance showed that the final model predictions are relatively insensitive to the remaining statistical uncertainty in the optimized kinetic parameters within the investigated operating range. The resulting parameter-propagated uncertainty intervals were generally small compared with the overall residual scatter. This suggests that the remaining deviations are unlikely to arise from poor statistical precision of the fitted parameters alone, but rather from experimental variability, differences between literature datasets, reactor-model idealizations, fixed literature rate constants, and limitations of the compact reaction network.

At the same time, the present study highlights important limitations in the available experimental basis. Most existing COS pyrolysis datasets report COS conversion and, in some cases, limited product information, but do not provide complete characterization of sulfur-containing intermediates and products. This restricts the ability to independently validate sulfur-mediated pathways, distinguish between alternative sulfur reaction routes, or confirm the extent to which unreported products influence the observed carbon and sulfur balances. Future experiments should therefore include improved sulfur-product speciation, better carbon and sulfur balance closure, and systematic variation of dilution, pressure, residence time, and inlet composition.

The resulting kinetic model is sufficiently compact for incorporation into reactor-scale and process-level simulations of high-temperature sulfur-containing gas streams, while retaining a clear interpretation of the dominant pathways controlling COS conversion. More broadly, the approach illustrates how heterogeneous literature data sets can be transformed into a simulation-ready kinetic model. Further progress will require targeted experimental datasets with improved sulfur-species characterization, as well as first-principles analysis of the less certain sulfur-mediated reactions and validation under conditions closer to industrial operation.

Author contributions

Klaus Jacobs: writing – original draft, visualization, validation, software, methodology, investigation, formal analysis, data curation, conceptualization. Soroush Zareghorbaei: writing – review & editing, methodology, visualization, validation, investigation, formal analysis, data curation. Jeroen Lauwaert: writing – review & editing, supervision, resources, project administration, conceptualization. Joris Thybaut: writing – review & editing, supervision, resources, project administration, funding acquisition, conceptualization.

Conflicts of interest

There are no conflicts to declare.

Data availability

The data supporting this article have been included as part of the supplementary information (SI).

Supplementary information is available. See DOI: https://doi.org/10.1039/d6re00101g.

Acknowledgements

This work was supported by the European Union's Horizon Europe research and innovation program under Grant Agreement No. 101058100 (e-CODUCT project). The authors gratefully acknowledge this funding support.

Notes and references

1 M. I. Stewart, in *Surface Production Operations*, Gulf Professional Publishing, 3rd edn, 2014, vol. 3, pp. 433–539.
2 P. D. Clark, N. I. Dowling, M. Huang, W. Y. Svrcek and W. D. Monnery, *Ind. Eng. Chem. Res.*, 2001, **40**, 497–508.
3 S. Renda, D. Barba and V. Palma, *Ind. Eng. Chem. Res.*, 2022, **61**, 5685–5697.
4 A. L. Kohl and R. B. Nielsen, in *Gas Purification*, Gulf Professional Publishing, 5th edn, 1997, pp. 670–730.
5 e-CODUCT – Greenhouse gas and acid gases conversion by electrothermal catalysis, https://e-coduct.eu/, (accessed 28 July 2025).
6 S. R. Batool, M. Fabbiani, A. Novikov, R. Ghassemi, S. Zareghorbaei, J. Lauwaert, L. Pinard, H. Retot, J. W. Thybaut and V. Valtchev, *Catal. Today*, 2026, **466**, 115660.
7 H. G. Schecker and H. G. Wagner, *Int. J. Chem. Kinet.*, 1969, **1**, 541–549.

8 A. J. Hay and R. L. Belford, *J. Chem. Phys.*, 1967, **47**, 3944–3960.
9 D. Woiki and P. Roth, *Ber. Bunsenges. Phys. Chem.*, 1992, **96**, 1347–1352.
10 K. Karan, A. K. Mehrotra and L. A. Behie, *Chem. Eng. Commun.*, 2005, **192**, 370–385.
11 K. Karan, A. K. Mehrotra and L. A. Behie, *Ind. Eng. Chem. Res.*, 1998, **37**, 4609–4616.
12 M. Oya, H. Shiina, K. Tsuchiya and H. Matsui, *Bull. Chem. Soc. Jpn.*, 1994, **67**, 2311–2313.
13 J. R. Partington and H. H. Neville, *J. Chem. Soc.*, 1951, 1230–1237.
14 F. Faraji, I. Safarik, O. P. Strausz, E. Yildirim and M. E. Torres, *Can. J. Chem. Eng.*, 1999, **77**, 78–84.
15 L. Nemeth, G. Gati, A. Gervasini, A. Auroux, G. Mink, I. S. Pap and T. Szekely, *Appl. Catal.*, 1990, **64**, 143–159.
16 B. Z. Dlugogorski, Z. Zeng, I. Oluwoye and M. Altarawneh, *SSRN Electron. J.*, 2022, DOI: 10.2139/SSRN.4123953.
17 A. Panda, P. A. Biswas, L. V. Simitz, J. W. Streicher, C. L. Strand and R. K. Hanson, *J. Phys. Chem. A*, 2026, **130**, 1384–1393.
18 R. W. Fair and B. A. Thrush, *Trans. Faraday Soc.*, 1969, **65**, 1208–1218.
19 S. Du, J. S. Francisco, B. C. Shepler and K. A. Peterson, *J. Chem. Phys.*, 2008, **128**(20), 204306.
20 M. Akimoto, H. Suto and H. Niiyama, *Bull. Chem. Soc. Jpn.*, 1986, **59**, 683–687.
21 L. A. Haas and S. E. Khalafalla, *J. Catal.*, 1973, **30**, 451–459.
22 L. Arnaut, *Chem. Kinet.*, 2021, 247–261.
23 S. W. Benson, *Thermochemical Kinetics: Methods for the estimation of Thermochemical data and rate parameters*, John Wiley & Sons, 1968.
24 G. A. Lara-Cruz and G. E. Moyano, *Theor. Chem. Acc.*, 2018, **137**, 1–17.
25 B. Peters, in *Reaction Rate Theory and Rare Events Simulations*, Elsevier, 1st edn, 2017, pp. 209–225.
26 J. Troe, *J. Chem. Phys.*, 1977, **66**, 4745–4757.
27 D. L. Baulch, M. J. Pilling, C. J. Cobos, R. A. Cox, C. Esser, P. Frank, T. Just, J. A. Kerr, J. Troe, R. W. Walker and J. Warnatz, *J. Phys. Chem. Ref. Data*, 1992, **21**, 411–734.
28 M. W. Chase and M. W. Chase, *NIST-JANAF Thermochemical Tables*, American Institute of Physics, 4th edn, 1998.
29 J. L. Bao, X. Zhang and D. G. Truhlar, *Phys. Chem. Chem. Phys.*, 2016, **18**, 16659–16670.
30 R. J. Hanrahan, *Comput. Chem.*, 1982, **6**, 21–25.
31 Z. Zeng, B. Z. Dlugogorski, I. Oluwoye and M. Altarawneh, *Proc. Combust. Inst.*, 2019, **37**, 677–685.
32 E. N. Fuller and J. C. Giddings, *J. Chromatogr. Sci.*, 1965, **3**, 222–227.
33 E. N. Fuller, K. Ensley and J. C. Giddings, *J. Phys. Chem.*, 1969, **73**, 3679–3685.
34 E. N. Fuller, P. D. Schettler and J. C. Giddings, *Ind. Eng. Chem.*, 1966, **58**, 18–27.
35 G. Froment, K. Bischoff and J. De Wilde, *Chemical Reactor Analysis and Design*, 2011, pp. 505–584.
36 A. B. Callear, Basic RRKM Theory, *Comprehensive Chemical Kinetics*, Elsevier, 1st edn, 1983, ch. 4, vol. 24, pp. 333–356.